Original Article

Combined effect of tungsten inert gas welding and roller expansion processes on mechanical and metallurgical characteristics of heat exchanger tube-to-tubesheet joints

Dinu Thomas Thekkuden [a], Abdel-Hamid Ismail Mourad [a,b,c,*], Tholkappiyan Ramachandran [a], Abdel-Hakim Bouzid [d], Ravi Kumar [e], Ahmed Alzamly [f]

[a] Mechanical and Aerospace Engineering Department, College of Engineering, United Arab Emirates University, Al-Ain, P.O. Box. 15551, United Arab Emirates
[b] National Water and Energy Center, United Arab Emirates University, Al-Ain, P.O. Box. 15551, United Arab Emirates
[c] On Leave from Mechanical Design Department, Faculty of Engineering, El Mataria, Helwan University, Cairo, Egypt
[d] Ecole de Technologie Superieure, 1100 Notre-Dame Quest, Montreal, Quebec, H3C 1K3, Canada
[e] Dept. of Metallurgical r Materials Engineering, Indian Institute of Technology Madras (IIT Madras), Chennai, 600036, India
[f] Department of Chemistry, College of Science, United Arab Emirates University, Al Ain P.O. Box 15551, United Arab Emirates

ARTICLE INFO

ABSTRACT

Tube-to-tubesheet joints are one of the major vulnerable locations prone to cracks in heat exchangers. The manufacturing processes of these joints have an important role in providing structural integrity to the heat exchangers. The main objective of this work is to study the impact of the combined effect of tungsten inert gas weld and expansion percentages of 3%, 5% and 7% on the structural integrity of carbon steel-based tube-to-tubesheet joints. The results show that the pull-out strength of hybrid welded and expanded using 3%, 5% and 7% expansion percentages has exceeded the tube axial strength. The minimum leak path of the welds was satisfactorily above two-thirds of the tube wall thickness. Vickers hardness was restricted at the adjacent regions of weld to below 250 HV. The microstructural studies indicate that the higher the expansion percentage, the smaller the grains at the inner tube surface and the higher the extent the fine grains formed from the inner tube surface. The effect of expansion on the grains at the inner and outer tube surfaces of the transition zone and the unexpanded zone was found negligible. The

absence of grain refinement on the outer tube surface using light expansion at a 3% expansion percentage indicated that the contact pressure was inadequate on the tube-to-tubesheet interface. The hardness at the expanded zone and transition zone of the inner tube surface was higher than at the outer tube surface due to the plastic deformation caused by the intensive roller expansion pressure.

1. Introduction

The structural integrity of tube-to-tubesheet joints in shell and tube heat exchangers has a crucial role in separating the tube-side and shell-side transfer fluids operating at different temperatures and pressures. Inadequate manufacturing processes, improper welding parameters, insufficient wall thinning percentages, the corrosiveness of process media, tube and tubesheet materials adversely affect the strength of the tube-to-tubesheet joint [1]. Several reported cases of heat exchanger failures caused by fractures at the tube-to-tubesheet joints during the last decades have highlighted the relevance of the structural integrity of the tube-to-tubesheet joints (TTTJ) in shell and tube heat exchangers. The malfunctioning of the shell and tube heat exchangers in nuclear power plants, marine applications, power generation stations, pharmaceuticals, refrigeration and air conditioning results in a huge economical loss. The cracks at the tube-to-tubesheet joints are highly influenced by the manufacturing techniques and process parameters. According to Xu et al., the major reason for the collapse of the heat exchanger used for dimethyl ether-propylene project was the residual tensile stresses at the seal welded joints where the presence of high chloride content in the polluted pre-steam during start-up operation has aggravated the stress corrosion cracking at the seal welds [2]. Stress corrosion cracking is a common phenomenon in carbon steels exposed to brine and contaminated process media [3]. The corrosion or pitting causes abrupt decrease in the tube wall thickness provoking the leakage [4]. Yang et al. found a lack of seal expansion in a spiral wounded heat exchanger as the main reason for ceasing the functioning of nuclear power plant heat exchanger [5]. On the contrary, Xu et al. have found that the high tensile residual stresses induced in the TTTJ by seal expansion have caused the failure of the heat exchanger [2]. Adullah and Ezuber revealed that the poor workmanship of welding the tube-to-tubesheets and stress corrosion cracking are the causes of the premature breakdown of gas/steam heat exchanger in a gas plant [6]. The failure analysis of a cracked heat exchanger in a coastal nuclear power plant conducted by Gong et al. revealed the pre-existing mechanical damages imparted by the mishandling of drawing heads while installation eventually lead to crack formation and propagation causing leakage at the tube-to-tubesheet joint [7]. The main causes of a failed shell and tube heat exchanger, according to Liu et al., were bad welding and inappropriate expansion accompanied by resonant vibration [8]. Huang et al. reported that the tube-to-tubesheet (TTT) welds in steam generators of CPR1000 units

have been damaged by loose parts [9]. The TTT welds exposed to galvanic corrosion and hydrogen embrittlement cracking caused the nitric acid loop heat exchanger to cease operation unexpectedly [10]. Corleto and Argade reported similar sulphide-assisted stress corrosion cracking at the dissimilar carbon steel tube to duplex stainless steel tubesheet welds in the heat exchangers used for the H_2S application [11]. The high residual stresses in the tube-to-tubesheet welded joints favour the propagation of fatigue cracks induced by the resonant vibration [8]. Sui et al. reported that the welding residual stress at the TTTJs and caustic concentration has caused the leakage by developing caustic stress corrosion cracking [12]. The review article by Thekkuden et al. discussed many instances of premature heat exchanger failures caused by the induced stresses at the TTTJs [13]. Based on the literature, the major reasons for the collapse of heat exchangers are poor workmanship, corrosiveness of media, vibration, residual stresses due to mechanical and thermal actions. These failures proved the significance of tube-to-tubesheet joints in adding structural integrity to the heat exchangers.

The mechanical and thermal stresses at the tube and adjacent tubesheet region are influenced by the manufacturing processes. The expansion of the tubes induces mechanical residual stresses whereas the welding causes thermal stresses in and around the joints. The extent of stress depends on the process parameters of the manufacturing processes. The expanded zone and, transition zone separating the expanded and unexpanded zones in the tubes are the major regions affected by the residual stress-attributed defects [14,15]. The main manufacturing processes of tube-to-tubesheet joints are the expansion and welding of the tubes. The choice of the TTTJ fabrication techniques in industrial practice such as heavy expansion, welding, hybrid welding followed by light expansion, hybrid welding followed by heavy expansion and hybrid light expansion followed by welding solely depends on the engineering design of heat exchangers based on the operating temperatures and pressures of heat exchangers. Roller expansion and hydraulic expansion are commonly employed for expanding the tubes in which the tubes are subjected to elastic and plastic deformation. In the case of the welding process, manual gas tungsten arc welding (GTAW) or automated orbital gas tungsten arc welding are used commonly to join the TTT. For those heat exchangers operating at higher temperature and pressure, tube-to-tubesheet joints made of both welding and expansion, either hybrid welding followed by expansion or hybrid expansion followed by welding are recommended for strengthening and sealing the joints. In the hybrid joining processes, there is still uncertainty in the selection of the percentage of expansion as

Table 1 – Chemical composition of ASTM A179 Tube from optical emission spectroscope.

Element	C	Mn	Si	S	P	Cr	Ni	Cu	Ti	Al
%	0.112	0.473	0.217	0.0029	0.0089	0.0664	0.0213	0.0206	0.0022	0.0240
Element	N	Mo	V	Nb	W	Pb	Sn	As	Zr	Bi
%	0.0094	0.0046	<0.0005	0.0025	0.0071	0.0166	0.0042	0.0036	<0.0010	0.0069
Element	Ca	Sb	Se	Te	Ta	N	Zn	Co	Fe	CEV
%	0.0015	0.0396	0.0042	0.0182	<0.007	0.0094	<0.001	<0.001	98.9	0.208

there is a need for an optimum condition for avoiding failures. A higher expansion percentage increases the residual stress whereas an inadequate expansion percentage results in loose joints in hybrid welded and expanded TTTJs.

The mechanical and metallurgical properties of tube-to-tubesheet joints are dependent on the expansion percentages, grooves in the tube hole and welding parameters and design configurations. The grooves in the tubesheet hole enable the tube to bulge inwards to the groove during the tube expansion process. This bulged tube into the grooves acts as an interlocking mechanism that helps to resist the slipping of the tubes and to increase joint strength. Grooves are recommended for 'strength expansion' where the tubes are expanded with high expansion percentages [16]. It is worth noting that the grooves play a crucial role only during the tube expansion process whereas the weld strength is unaffected by the presence of grooves. Massey and Jones found out that double grooves are more effective in increasing the tube pull-out strength whereas, the difference in the tube pull-out strength of single grooved and grooveless tubesheet is minimal [17]. Thekkuden et al. agreed that double-grooved joints are effective at higher expansion pressures for providing adequate joint strength whereas the joint strength is considerably reduced due to less tube bulging towards the double grooves using light expansion percentages [18]. In addition, Massey and Jones also found out that the 3 roller expanders have imparted higher tube pull-out strength compared to 5 roller expanders for a fixed rolling torque while expanding titanium tubes towards the brass tubesheet [17]. Allam and Bazergui estimated the tube pull-out strength of around 6000 N for the 2.2 mm thick Inconel 690 tube that was having 19.05 mm outer diameter and 16.764 mm inner diameter with 25 mm thick and 19.34 mm drilled hole SA 508 tubesheet manufactured by a hydraulic expansion process [19]. They reported that the axial strength of the rolling expanded joints increases with the increase in the radial clearance between the tube and tubesheet and strain hardening behaviour using numerical analysis. In the experimental analysis conducted by Haneklaus et al. for comparing the roller expanded and roller expanded followed by the diffusion welding process, the tubes were pulled out from the roller expanded tube-to-tubesheet joints whereas the tubes were fractured before

being pulled out from the joints in the case for roller expanded followed by diffusion welding process during the tube pull-out tests [20]. Ma et al. experimentally evaluated that the general trend of increasing tube pull-out strength with the expansion percentage depends on the tube materials after identifying an apparent fall in the tube pull-out strength at an 8% tube expanding percentage in S304 tubes [21]. For the hydraulic expansion process, Thekkuden et al. found a similar trend of increase in the tube pull-out load with the rise in the expansion percentages from 240 MPa to 340 MPa [22]. Wei and Ling reported that the welding configuration of tube-to-tubesheet joint with protruded tube and tungsten inert gas (TIG) fillet welding was found to have higher tube pull-out force compared to v-grooved, u-grooved and flush joints [23]. These literatures indicate that the design of tube-to-tubesheet joints is complex with several joint configurations, designs and manufacturing process parameters. Therefore, a proper comparative study of processing techniques is inevitable and demanded.

Research articles on the experimental assessment of tube-to-tubesheet joints compared to the numerical and analytical evaluations of tube-to-tubesheet joints are rare. Furthermore, studies focussing on the hybrid welded and expanded tube-to-tubesheet joints are lacking in the literature. In addition, the evaluation of the effect of welding and expansion percentages in roller expansion on the mechanical and metallurgical characteristics of hybrid welded-expanded tube-to-tubesheet joints is highly demanded. This study proposed the mutual effect of welding and roller expansion percentages (3%, 5% and 7%) on producing quality welded joints.

2. Experimental procedure

The tube-to-tubesheet joints made of ASTM A179 tube and SA 266 grade 2 tubesheet are investigated using a machined mock-up tubesheet block. Table 1 and Table 2 provide the estimated chemical compositions of ASTM A179 and SA 266 grade 2 obtained using optical emission spectroscopy. The dimensions of the mock-up tubesheet for producing hybrid welded-roller expanded joints are 161 mm × 212 mm × 62 mm. A Mock-up tubesheet block with thirty-five double

Table 2 – Chemical composition of SA 266 Gr.2 Tubesheet from optical emission spectroscope.

Element	C	Mn	Si	S	P	Cr	Ni	Cu	Ti	Al
%	0.173	1.44	0.392	0.0025	0.0074	0.0104	0.150	0.0134	0.0023	0.0370
Element	N	Mo	V	Nb	W	Pb	Sn	As	Zr	Bi
%	0.005	0.0963	0.0148	0.0214	0.0090	0.0186	0.0029	0.0070	0.0012	0.0081
Element	Ca	Sb	Se	Te	Ta	B	Zn	Co	Fe	CEV
%	0.00099	0.0420	0.0052	0.0201	<0.007	0.0013	<0.001	<0.001	97.5	0.448
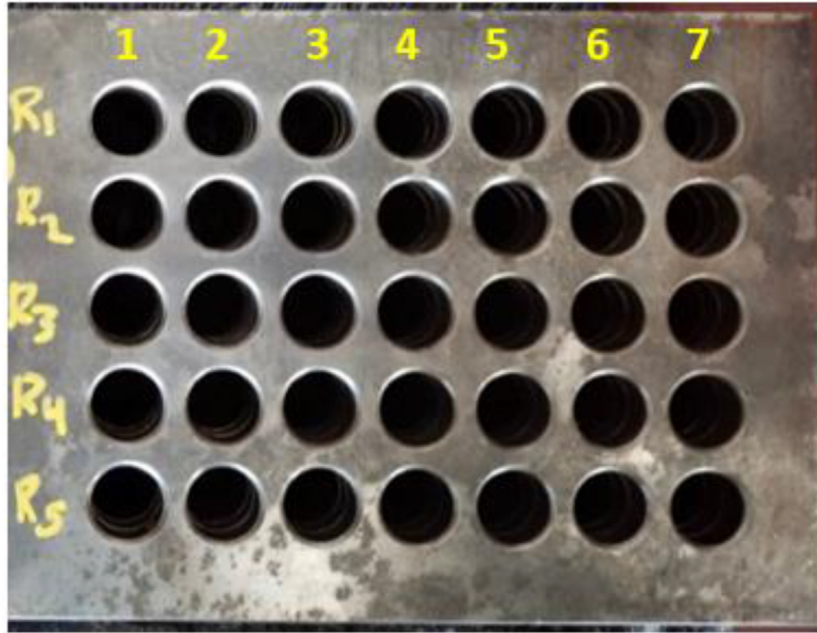
Fig. 1 — Mock-up tubesheet block.

grooved tubesheet holes with a tube pitch of 25.4 mm was manufactured as shown in Fig. 1. Two grooves are manufactured on the tube hole for enhancing the strength by the tube expansion process in hybrid welded-expanded joints. The tubes were arranged with a 3 mm protrusion configuration. The tubes have a standard size of 19.05 mm outer diameter with 2.11 mm thickness. Fig. 2 shows the engineering drawing of welded-expanded tube-to-tubesheet joints. For the welding of tube to tubesheet, gas tungsten arc welding was performed using EWM TETRIX 421 AC/DC COMFORT activArc power-source and ER 80SNi-1cosumable. The chemical composition of ER 80SNi-1 welding rod is shown in Table 3. The welding was performed at ambient atmospheric temperature with two welding passes — one root pass and one cap pass. 130 A
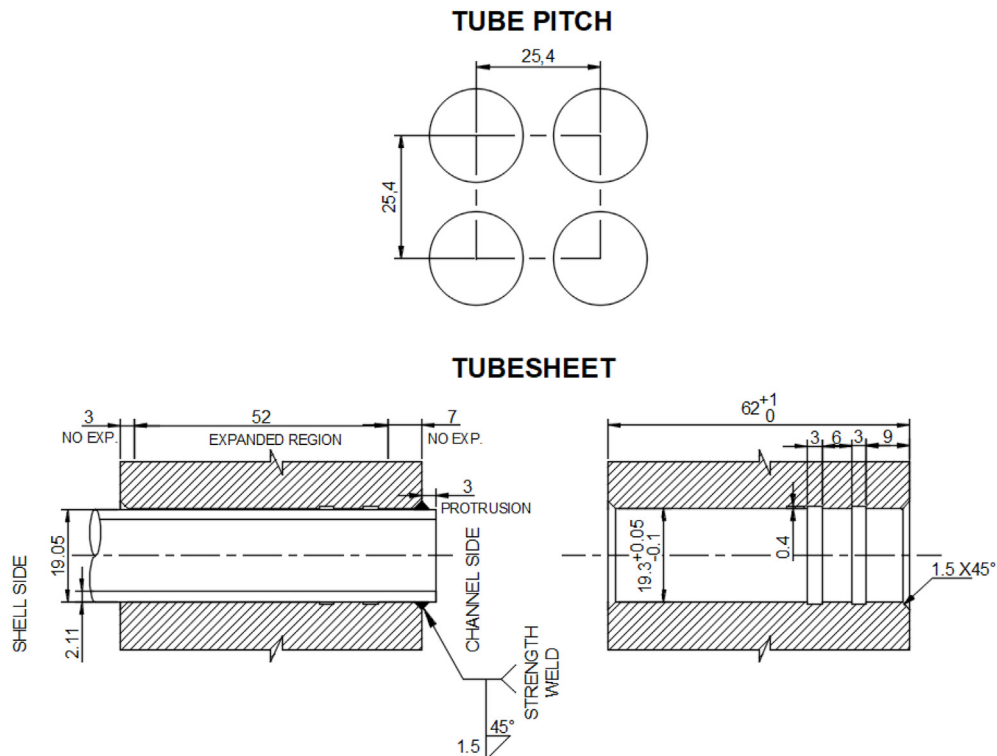
Fig. 2 — Sketch of welded and expanded tube-to-tubesheet joint and tube pitch.

Table 3 — Chemical composition of ER 80SNi-1.

Element	C	Cu	Mn	Mo	Ni	P	Si	S
(%)	0.10	0.12	1.10	0.10	1.00	0.01	0.60	0.01

current, 12.4 V voltage, consumable rod with a diameter of 1.6 mm, direct current electrode negative (DCEN) configuration, uphill progression and constant 99.997% pure Argon shielding gas with a flow rate of 28 cfh are the chosen welding parameters for tungsten inert gas welding of tube-to-tubesheet welds. The welding setup is shown in Fig. 3. The rolling expansion is performed using Maus Italia Quadrol 90 comprising of F90V3 electronic expansion control unit, expander and articulated telescopic shaft (Fig. 4). The mock-up TTJs are inspected for qualifying the tube-to-tubesheet joints using a liquid penetration test, gamma ray radiographic examination, macro examination, micro examination, minimum leak path, pull-out test and hardness test. Tubes in the second hole (Row 2-hole 2), fourth hole (Row 2-hole 4) and sixth hole (Row 2-hole 6) of the second row were expanded at 7%, 5% and 3% expansion percentages whereas the tubes placed in all the remaining tube holes were expanded with light expansion (nearly 3%). Light expansion of the remaining tubes was selected to incorporate the influence of neighbour hole expansion on 3%, 5% and 7% expanded joints [24,25]. Table 4 illustrates the dimensions before and after the rolling operation for definite expansion percentages of welded-expanded joints. A standard non-destructive liquid penetration test has been performed by applying penetrant and developer on all the welds. Gamma-ray radiographic examination using Iridium 192 has been carried out on sectioned mock-up welded and expanded joints with the procedure complying with AWS D1.1:2015 Ed. The macro examination is performed in accordance with the standard ASME section IX

Ed. 2019. Acceptance standard ASME SEC. IX Ed. 2019-QW-193.1.3 or API 660 (9.5.7(a)) are used for qualifying seven numbers of tube-to-tubesheet weld joints (seven joints on row 4) by measuring the weld throat for the minimum leak path. Pull-out tests are conducted on the tube-to-tubesheet joints that are expanded at 3%, 5% and 7% expansion percentage and qualification is assessed based on ASME SEC. VIII DIV. I ED. 2019 - Appendix A. Vickers hardness at the weld zone, heat affected zone and base material are measured using a test load of 10 kgf and a square-based diamond pyramid indenter. The vickers hardness measurements at the base material, weld and heat affected zone are compared with the NACE MR0175 standard for the acceptance criteria. Vickers hardness at the inner and outer tube surfaces at the expanded zone, transition zone and unexpanded zone was measured by applying 30 kgf force. The macrographic and microscopic examinations of welds were conducted for estimating the minimum leak path and microstructures, respectively. Samples for optical macroscopic observations were ground using P120, P180 and P240 grid waterproof silicon carbide (SiC) paper followed by cloth polishing. For optical microscopic analysis, samples were ground with P120, P240, P320, P600, P1000, P1200, P1500 grid SiC papers followed by cloth polishing with 6 μm and 3 μm diamond particles. The polished mirror-like samples were washed with pure ethanol followed by etching with 2.5% Nital (97.5 ml ethanol + 2.5 nitric acid) for 30s etchant time. The ASTM grain sizes of base materials, heat affected zones of tube and tubesheet, and inner and outer tube cross-sections are measured using Heyn intercept method. Microstructures of the weld coupon were monitored by a JEOL JSM-6010LA scanning electron microscope (SEM, Akishima, Tokyo, Japan) at 1000× magnification. Fields of the sample were inspected under a high-vacuum (ULVAC KIKO lnc, Model: G-100DB, Miyazaki, Japan) and micrographs of the
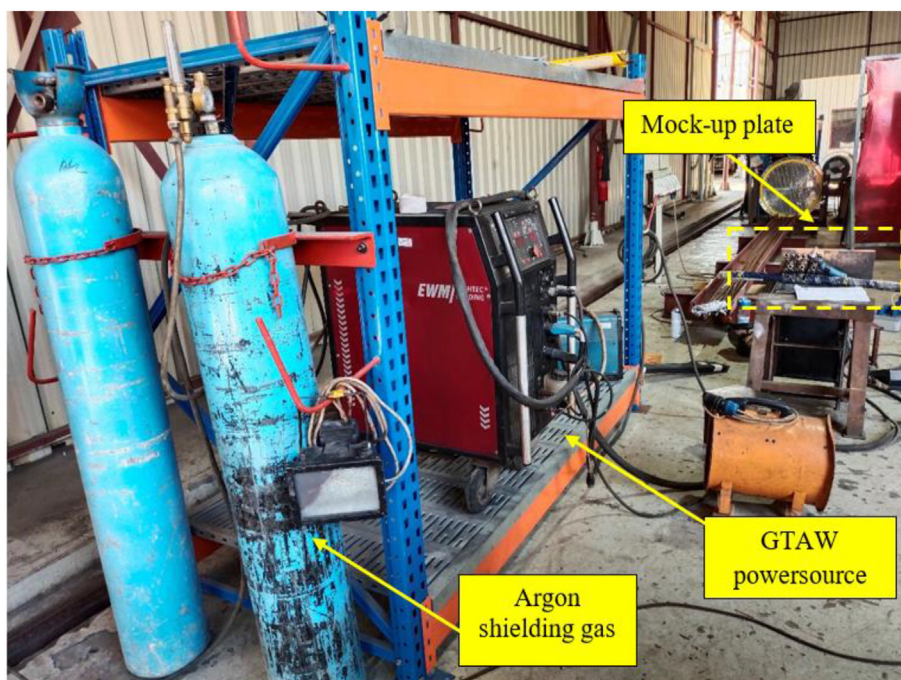
Fig. 3 — Gas tungsten arc welding setup for welding tube-to-tubesheet joints.
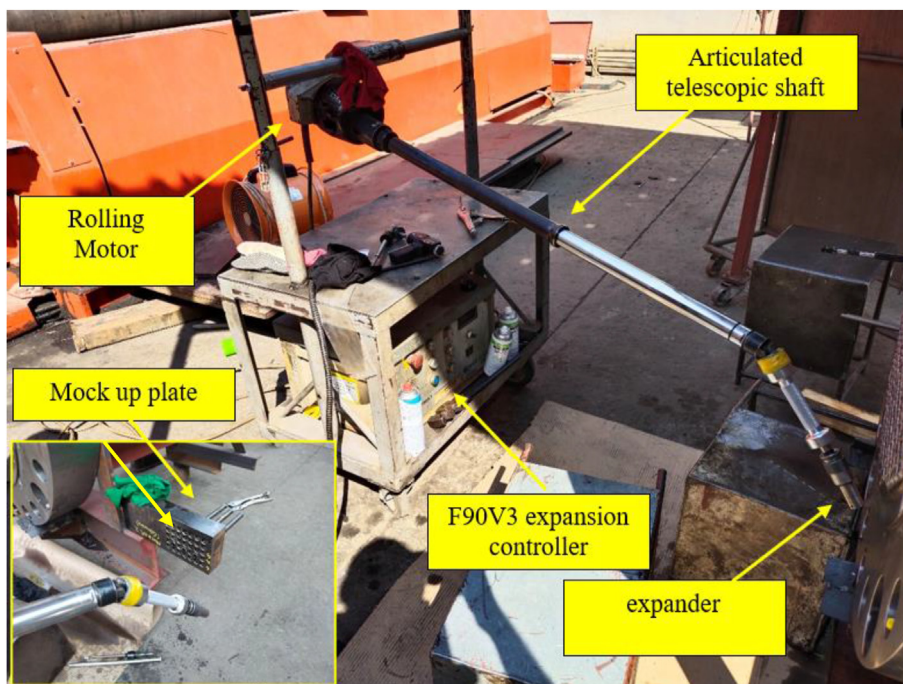
Fig. 4 – Roller expansion setup for expansion of welded tubes.

sample were recorded using InTouchScope JSM software. X-ray diffraction (XRD) of the weld metal for phase identification was evaluated using a SHIMADZU Lab X-XRD-6100 X-ray diffractometer with Cu-Kα X-ray line ($\lambda = 1.5418$ Å) running at 40 kV with a current of 30 mA. The profiles were recorded over the 20°–100° range with a 0.02°/min step size. For phase identification, the XRD profiles were screened against the PDF-2 database (ICDD).

3. Results and discussion

3.1. Non-destructive tests

The liquid penetrant test complying with the requirement of ASME Section V, Article 6 and ASME, IX QW-193.1.2 is mandatory for qualifying tube-to-tubesheet welds [26]. The inspected tube-to-tubesheet joints using the liquid penetrant test are shown in Fig. 5. The welds were free from linear and rounded indications. The lack of red indications on the coated developer on the weld surface proved that all thirty-five welds were free from the welding surface defects. However, the liquid penetration test is limited only to the identification of surface defects. Macro examination of weld cross-sections

after sectioning the fourth row of mock-up TTTJs is performed for examining the presence of voids between the root and cap pass, weld porosities on the sectioned surface and minimum leak path.

A coupon from the mock-up was sectioned as shown in Fig. 6 and examined using Iridium-192 gamma ray for radiographic inspection. Indications of weld porosities, blow holes, discontinuities and cracks were absent in the radiographic film shown in Fig. 7. The circular line between the tube and the tubesheet is the indication of the clearance gap between the tube and the tubesheet. This clearance gap was present to a depth of 7 mm from the tubesheet surface exposed to welding. In this case of welding followed by tube expansion, the tube expansion starting from the weld joint (tube end) and on the weldment would result in causing the formation of cracks at the welds. To mitigate this problem, the tube expansion was carried out starting from 7 mm away from the tubesheet end (Refer to Fig. 2) in such a way as to have no impact of tube expansion on the weldments. In addition, the burn-through defect as a result of excessive heat input that would have caused the melting of the tubes was found absent. The welds are concluded as qualified with free of weld defects. The welding expertise and welding parameters are found appropriate for the welding of tube-to-tubesheet joints. In this

No.	Tube designation	Tube OD, D0	Tube ID Before Expansion, d1	Tube ID after Expansion, d2	Tube Hole Diameter, h	Tube wall reduction Percentage, k
		mm	mm	mm	mm	%
1	Row 2- hole 2	19.04	14.56	15.15	19.30	7.37
2	Row 2- hole 4	19.05	14.55	15.03	19.30	5.11
3	Row 2- hole 6	19.05	14.55	14.95	19.31	3.11

Table 4 – Dimensions before and after the rolling operation for various expansion percentages.
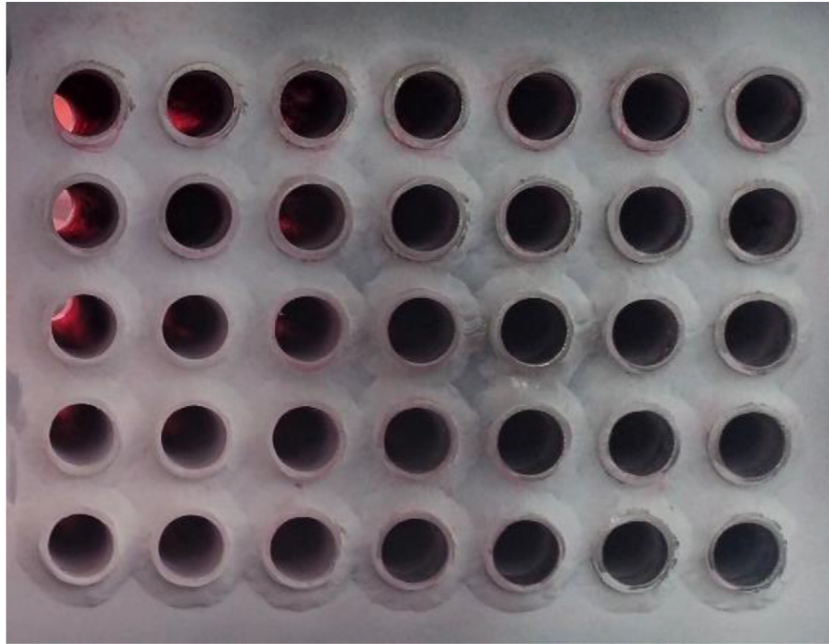
Fig. 5 — Qualified tube-to-tubesheet joints using non-destructive liquid penetrant test.

research, even though a section of the mock-up is used for radiography, it is recommended to conduct the radiographic inspection for the entire mock-up block immediately after the welding and tube expansion process.

3.2. Macro analysis

The tube-to-tubesheet joints from the fourth row are sectioned as shown in Fig. 8 for macro examining the welded-expanded TTTJs. Fig. 9 shows the corresponding macro images of hybrid welded-expanded mock-up tube-to-tubesheet joints. The macro evaluation indicated that all the welds were free from porosities and slag impurities. The weld profiles were excellent and acceptable with good fillet weld bead characteristics. Excellent penetration and sidewall fusion of all the welds to the base materials were evident from the macrostructures. There was an excellent fusion between the layers of weld metal deposited by the final cap pass over the root pass. No voids were visible between the cap and root pass. In addition, there is no evidence of burning through defect in the tube wall thickness. Therefore, the macro examination of tube-to-tubesheet welds proved that the welds were free from

internal defects. The TTTJs are concluded as quality joints produced using appropriate weld parameters.

3.3. Minimum leak path

The minimum leak path is estimated for the welds from the macro images inspected at $10\times$ magnification. Table 5 provides the measured minimum leak path for seven welds from the fourth row of the mock-up block. The qualification of welds was assessed based on the clause QW-193.1.3 (a) and (e) (Acceptance Criteria — Macro-Examination, Tube-to-tubesheet tests) in ASME section IX, 2004 edition [27]. According to QW-193.1.3, the welds are qualified if the weld throats are not less than two-thirds of the tube wall thickness and free from defects upon macro inspection at $10\times$ magnification. The tube wall thickness of SA 179 tube is 2.11 mm and two-thirds of the tube thickness is 1.4 mm. The measured weld throat or minimum leak path of the seven weld joint measurements is greater than 1.4 mm. Since the minimum leak path is the shortest route for the leak to occur, the weld throat measurement greater than 1.4 mm proved that the welds are qualified based on ASME Section IX, clause QW-193.1.3.

Fig. 6 — Coupon for radiographic inspection.
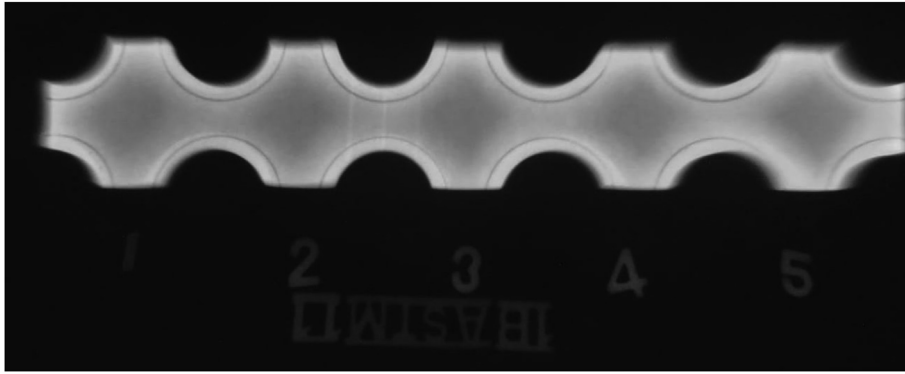
Fig. 7 — Radiograph from radiographic inspection of coupon using Iridium-192 gamma ray.

Furthermore, stringent rules for qualifying the minimum leak path compared with the tube thickness are in industrial practice according to the design code set forth by the manufacturer. In this study, all the weld throat leg measurements are greater than the 2.11 mm tube thickness. Therefore, the minimum leak path of welds was qualified based on the tube thickness as well as based on the two-thirds of tube thickness criterion.

3.4.   Tube pull-out strength

Tube pull-out tests based on ASME Sec-VIII, DIV-1, Non-Mandatory Appendix A, Basis for Establishing Allowable Loads For Tube To-Tube-sheet Joints are used for qualifying the strength of TTTJs [28]. Fig. 10 shows the tube pull-out specimens sectioned from the mock-up block before conducting the tube pull-out test. Figs. 11 and 12 show the top and inclined views of fractured tubes after the tube pull-out test, respectively. The stress versus strain diagram and load versus displacement obtained from the tube pull-out test are shown in Fig. 13. The peak tube pull-out load of welded-expanded TTTJs at various tube wall reduction percentages of 3%, 5% and 7% were found to be 41.35 kN, 42.29 kN and 42.19 kN respectively. There was no clear significant marginal difference in the tube pull-out loads for the welded specimens further expanded with 3%, 5% and 7% expansion percentages. The major reason for the closeness of tube pull-out loads is that the fracture occurred at the tubes away from the tubesheet and tube-to-tubesheet joint in all three cases. Moreover, there was neither physical evidence of tube slippage nor the presence of weld cracks indicating the movement of the tube away from the tube-to-tubesheet joint under the action of pull-out force. Due to the phenomenon of fracture at the tubes

rather than at the welds, the resulted tube pull-out load represented the actual load-bearing capacity of the tubes rather than the strength of tube-to-tubesheet joints. The stress-strain and load-displacement graphs of two A 179 tubes from the tensile test results were plotted in Fig. 14. The average peak load and average tensile strength of the tubes were 42.36 kN and 377.27 MPa, respectively. The trend in the load-displacement graph represented the actual performance of the tube rather than the performance of the joint. Therefore, the maximum strength of 368 MPa, 378 MPa and 376 MPa for the hybrid welded and expanded joints with 3%, 5% and 7% expansion percentages represented the tensile strength of the tube. The tube fracture rather than the tube pulled out from the tube-to-tubesheet joint proved the presence of sufficient joint strength. The joint strength of hybrid welded and expanded joints with 3%, 5% and 7% expansion percentages clearly exceeded their respective axial tube strength. This clear indication of joint strength greater than the axial strength of the tube proved that the tube-to-tubesheet joints are qualified based on the ASME Section VIII Divisions 1 and 2 [29]. In the case of hybrid welding-expansion, the strength is imparted by both welding and expansion processes. In addition, the design configuration of the weld joint for the current experimental evaluation is chosen for achieving the strength weld. The fracture at the tubes indicated that the welded tube-to-tubesheet joints fall under the category of the full-strength weld which is defined as 'the design strength is equal or greater than the axial strength of the tube' in the clause UW-20.2 (a) in ASME section VIII-Division 1 [28]. In addition, the criteria for full-strength weld according to clause UW-20.6(c)(1) is achieved if the length of the combined weld legs measured parallel to the longitudinal axis of the tube at its outside diameter (a_c) shall not be less than the greater of the
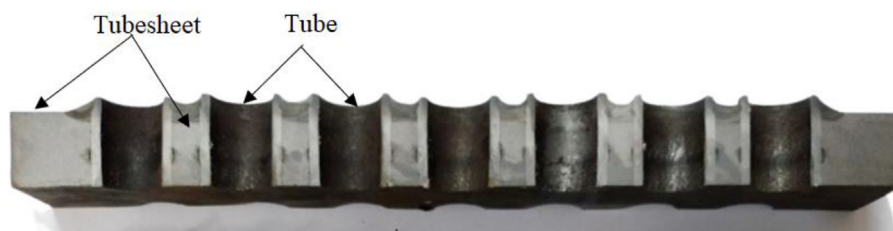
Fig. 8 — Etched and polished cross-sectioned samples for macro inspection.
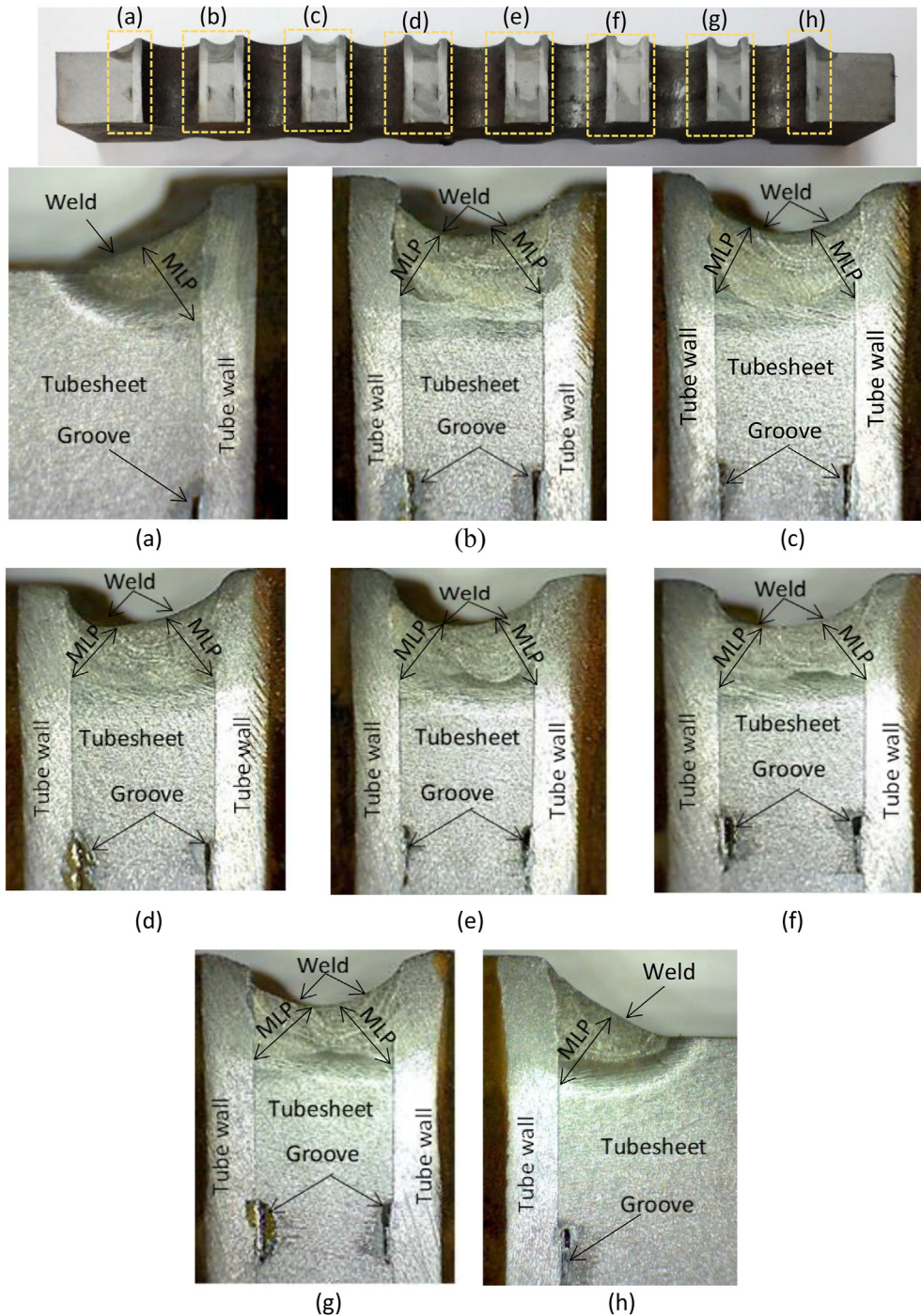
Fig. 9 − Macro images of sectioned tube-to-tubesheet joints from row 4 at 10× magnification. Row 4 (a) Tube 1 Side A (b) Tube 1 Side B and Tube 2 Side A (c) Tube 2 Side B and Tube 3 Side A (d) Tube 3 Side B and Tube 4 Side A (e) Tube 4 Side B and Tube 5 Side A (f) Tube 5 Side B and Tube 6 Side A (g) Tube 6 Side B and Tube 7 Side A (h) Tube 7 Side B.

minimum required length of the weld legs (a_r) or tube wall thickness (t). The minimum required length of the weld legs, a_r is calculated using equation (1). The Weld length leg depends on the outer diameter of the tube (d_o), tube wall thickness (t), weld strength factor (f_w) and the ratio of design strength to tube strength (f_d). The weld strength factor is the ratio of allowable stress in the tube (S_a) to allowable stress in the weld (S_w) where S_w is the least of allowable stress in the

tube or tubesheet. The weld strength factor is equal to 1 since the allowable stress in the weld is considered as the allowable stress in the tube. The design strength should be equal to or greater than the axial tube strength for the case of strength welded tube-to-tubesheet joints. Therefore, the value of f_d is equal to 1. Using these values, the theoretical minimum weld leg length is 2.56 mm. The measured average weld leg length (a_c) is 5.275 mm. The full-strength weld joint is achieved as a_c

Table 5 — Minimum leak paths of tube-to-tubesheet joints.

Tube Designation	MLP (Side A)	MLP (Side B)	Qualification criteria	
	mm	mm	MLP >1.4 mm	MLP >2.11 mm
Row 4 Hole 1	2.65	2.69	Qualified	Qualified
Row 4 Hole 2	2.82	2.75	Qualified	Qualified
Row 4 Hole 3	2.76	2.72	Qualified	Qualified
Row 4 Hole 4	2.69	2.76	Qualified	Qualified
Row 4 Hole 5	2.76	2.72	Qualified	Qualified
Row 4 Hole 6	2.82	2.71	Qualified	Qualified
Row 4 Hole 7	2.79	2.81	Qualified	Qualified

equals 5.275 mm is not less than either of a_r equals 2.56 mm or 2.11 mm tube wall thickness. Therefore, adequate weld legs and sufficient minimum leak path in full-strength welded joints provided the required tube joint leak tightness and strength [29].

$$a_r = 2\left[\left((0.75d_o)^2 + 1.07t(d_o - t)f_w f_d\right)^{\frac{1}{2}} - 0.75d_o\right] \qquad (1)$$

where,

d_o is the outer diameter of the tube
t is the tube wall thickness
f_w is the weld strength factor
f_d is the ratio of design strength to tube strength.

The roller expansion length depends on the tubesheet thickness. As roller expansion length increases, the contact surface area of the tube to the tubesheet increases. The developed contact pressure on a larger surface area

enormously increases the tube pull-out strength. The theoretical pull-out force is directly proportional to the roller expansion length, the outer radius of the tube and contact stress between the tube and tubesheet as illustrated by equation (2). The use of a 62 mm thick tubesheet and 52 mm expansion rolling length was found to enhance the strength of TTTJs. In addition to expansion roller length, Sang et al. have found that the pull-out strength increases with the increase in the magnitude of the expansion percentage [30]. The absence of fracture at the joint proved that the tube pull-out strength of TTTJs is contributed by the synergistic effect of welding and rolling expansion process. It is concluded that the tube-to-tubesheet welding and 3% expansion with this design configuration were sufficient for a strengthened joint. In addition, welding provided a sealing to prevent the direct interaction of tube-side and shell-side fluid required for safe and reliable heat exchanger operation [31].

$$F = 2\pi\mu\sigma_c r_o l_e \qquad (2)$$

where,

μ is the coefficient of friction between the tube and tubesheet
σ_c is the contact stress after unloading the roller expander
r_o is the outer radius of the tube
l_e is the effective length of roller expansion

3.5. Metallurgical examinations

3.5.1. Weld microstructure

All the tube-to-tubesheet welds are unaffected by the tube expansion since the tubes are roller expanded starting at 7 mm away from the tubesheet end surface. Fig. 15 shows the sectioned tube-to-tubesheet joint coupon for inspecting the
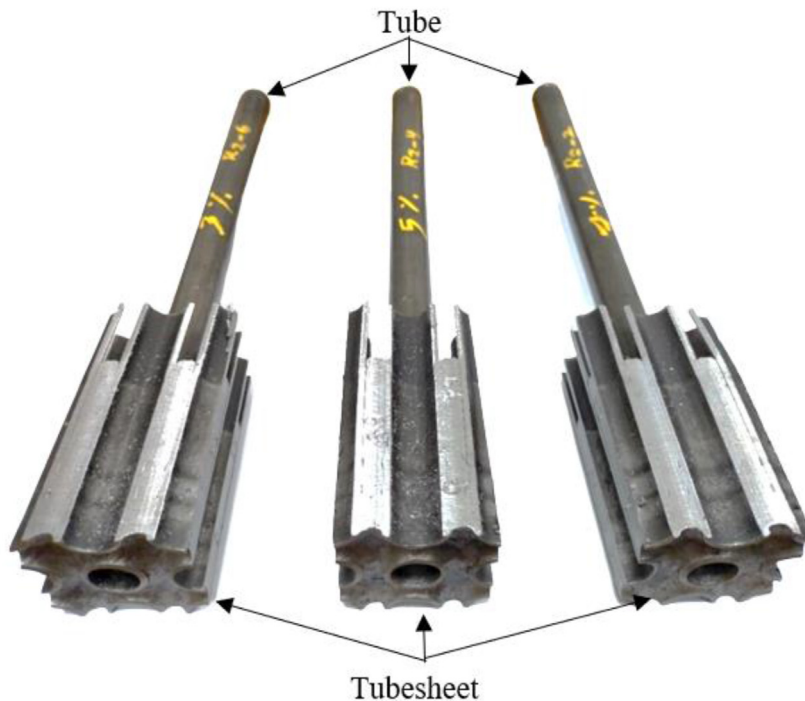
Fig. 10 — Tube pull-out specimens (before testing) — welded and expanded with 3%, 5% and 7%.
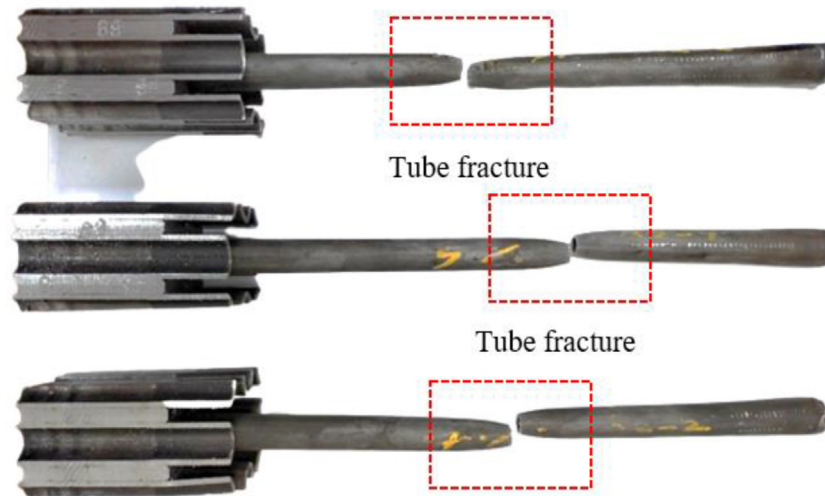
Fig. 11 – Fractured tube pull-out specimens (Top view) – welded and expanded with 3%, 5% and 7%.

welding metallurgy. Optical microscopic and scanning electron microscopic images are illustrated in Figs. 16–18 and Figs. 19–21 respectively. The sectioned surface exposed the tube, tubesheet, weld and heat affected zones in the tube-to-tubesheet joint. Fig. 16(a) and (b) illustrate the microstructure of ASTM A179 tube and SA 266 Gr. 2 tubesheet parent materials. The microstructure of ASTM A179 constitutes equiaxed polygonal ferrite (light area) and pearlite colonies (dark area) whereas the microstructure of SA 266 Gr. 2 comprises equiaxed ferrite (light area) and banded pearlite (dark area). The higher presence of ferrite in the microstructure of ASTM A179 tubes represented that the tube material belongs to low carbon steel material [32]. The presence of carbon (<0.3%) from the estimated chemical compositions of ASTM A 179 and SA 266 Gr. 2 materials proved the tube and tubesheet materials belong to low carbon steels. The typical behaviour of

ferrite structures is lower tensile strength and hardness compared to the pearlite structure [33]. Fig. 17(a) and (b) show the heat affected zone between the A179 tube and weld zone and SA 266 Gr.2 and weld zone respectively. The grains are coarser in the SA 266 gr. 2 and ASTM A 179 base materials compared to their heat affected zones. Tube A 179 base material exhibited grain size number ASTM 7 with a grain size of 31.8 μm whereas SA 266 Gr. 2 tubesheet indicated grain size number ASTM 8 with an average grain size of 22.5 μm. The heat affected zones are present at the tube and tubesheet due to the effect of welding arc heat dissipation and subsequent cooling. The microstructures of heat affected zones are the same as that of base materials, however, the grain sizes are very fine in the heat affected zones. The size of the grains at the heat affected zones of the tube and tubesheet are 9.4 μm (ASTM 10.5) and 7.9 μm (ASTM 11) respectively. The

Fig. 12 – Fractured tube pull-out specimens (inclined view) – welded and expanded with 3%, 5% and 7%.
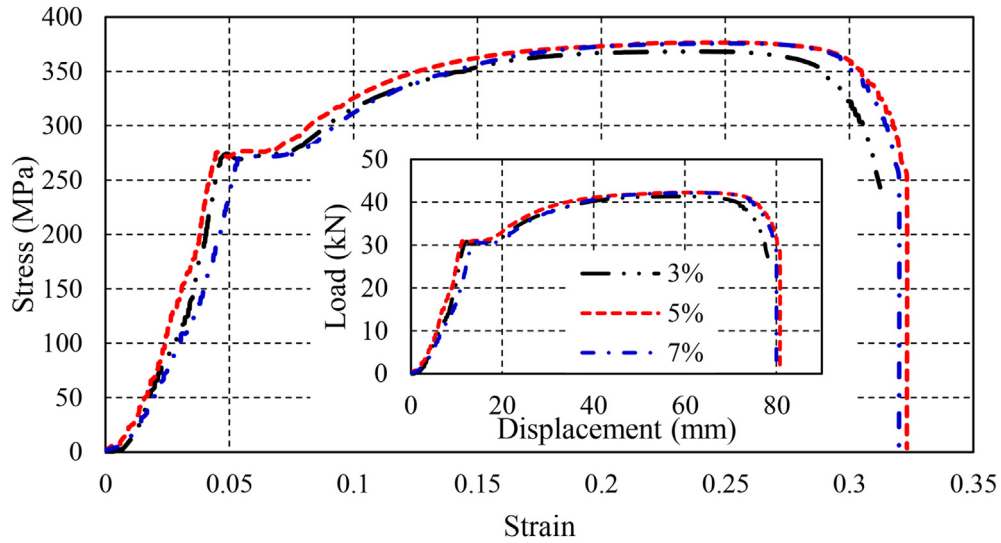
Fig. 13 — Stress-strain and load-displacement curves for welded-expanded Tube-to-tubesheet joints.

temperature in the heat affected zone which is not exceeding beyond the recrystallization temperature by a greater margin and the shorter recrystallization time for grains to grow are the reasons for the formation of fine grains in the heat affected zone [34]. Fig. 18 shows the microstructure of the fusion zone in the TIG welded tube-to-tubesheet joint. The microstructure of the weld fusion zone revealed polygonal ferrite, widmanstätten ferrite (WF) and acicular ferrite (AF). The saw tooth needle-shaped morphological form of ferrite emanating from the grain boundaries in the weld zone confirmed the presence of widmanstätten ferrite. The acicular ferrite with a larger proportion of ferrite and pearlite is formed at the fusion zone due to a slower cooling rate. Madariaga et al. [35] confirmed the evidence of the formation of acicular ferrite with pearlite and allotriomorphic ferrite in medium carbon steels with a 2 °C/s cooling rate based on a continuous cooling transformation diagram after austenitization at 1200 °C. The

heat input and cooling rate are critical in the phase transformation of ferrite in the TIG welding process [36]. The acicular ferrite in the fusion zone was a short ferrite needle with a basketweave appearance [37]. The XRD result of the sample from the weld zone shown in Fig. 22 confirmed the absence of δ-ferrite and γ-ferrite. The δ-ferrite phases usually forms in the fusion zone in TIG welding of carbon steel as a result of a rapid cooling process and by the presence of high carbon content as in medium and high carbon steel [38]. Table 6 provided the elemental composition of the weld zone estimated using optical emission spectroscopy. The weld zone belonged to low carbon steel as evident by the elemental carbon concentration of 0.116%, which was less than 0.3% (maximum percentage of carbon in low carbon steels). These low carbon content and slow cooling of the welds at ambient temperature have restricted the formation of delta phases at the tube-to-tubesheet weld zone. In addition, the major
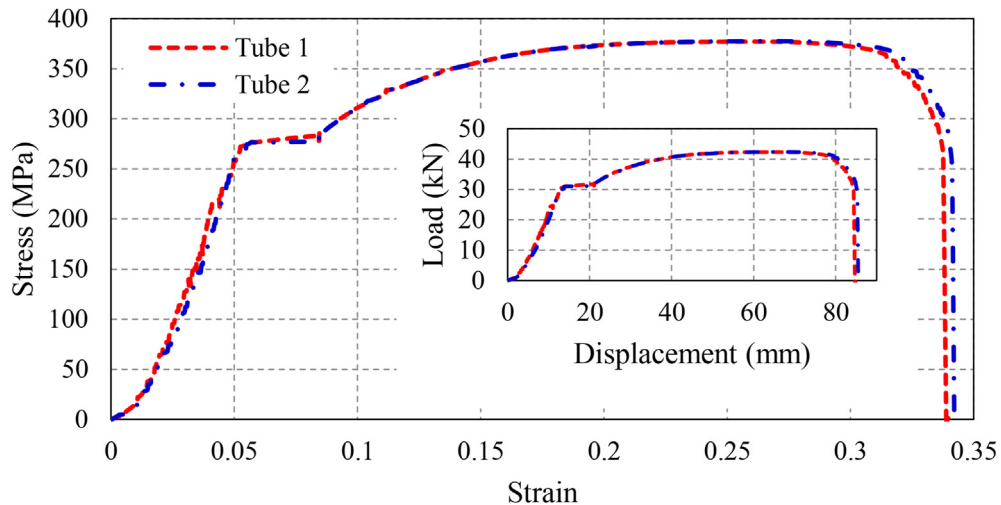
Fig. 14 — Stress-strain and load-displacement curves of A 179 tubes.
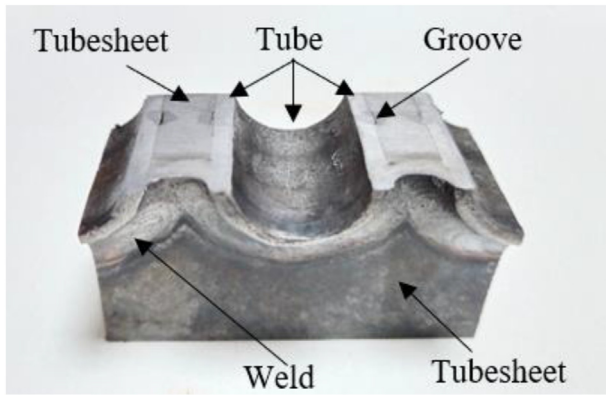
Fig. 15 − Sample for optical microscopic image.

alloying metals from the welding wire were found to be deposited at the weld zone. The weld zone comprised of nickel with 0.674%, manganese with 1.41% and silicon with 0.573% along with 96.7% Iron.

3.5.2. XRD analysis

XRD analysis was performed on the TIG welded tube-to-tubesheet joint for investigating the phases present at the weld zone. The peaks in the XRD plot indicated the presence of ICDD 98-008-8002 coded α ferrite. Three distinct peaks at $2\theta = 45.33°$ (011), $2\theta = 65.57°$ (002) and $2\theta = 82.83°$ (112) represented the presence of α ferrite. The delta ferrite (ICDD 98-005-1276) with peaks at $2\theta = 43.62°$, 63.39° and 80.11° and, austenite ferrite with peaks at $2\theta = 43.92°$, 51.17°, 75.28°, 91.48° and 96.84° were absent in the XRD plot. This proved the absence of delta ferrite and austenite ferrite in the welded TTJs. The absence of a rapid cooling rate and low carbon content inhibited the formation of delta ferrite and austenite ferrite [39].

3.5.3. Microstructures of the necked zone and expanded zone in tested tube pull-out specimens

The fracture occurred at the tube away from the joint in welded and 3%, 5% and 7% expanded tube-to-tubesheet joints. The strength of the tube-to-tubesheet joints is greater than the axial strength of the tubes. However, there are chances for

tube displacement or slippage from the welded tube-to-tubesheet joint. Fig. 23 shows the microstructures of the tube at the necked region and expanded zone. The grains are elongated at the necked tube region along the tensile direction due to intense plastic deformation and necking [40]. On the contrary, the grains at the expanded zones of the tube near the weld zone were equiaxed in 3%, 5% and 7% expanded conditions. The absence of grain elongation in the expanded zones for the three cases proved that the adjacent region around the expanded zone has been unaffected during the pull-out test. This proved the hybrid welded and expanded tube-to-tubesheet joints are of sufficient structural integrity and joint strength.

3.5.4. Microstructures of plastically deformed tubes

The inner surface of the tubes was subjected to expansion using rollers in a radially outward direction. The initial expansion pressure exerted by the rollers was used to initiate the contact between the tube and tubesheet at the expanded zone by reducing the clearance gap with tubes undergoing both elastic and plastic deformation [14]. After the initial contact, the continued rolling force compressed the tube against the tubesheet causing the plastic deformation aided tube wall reduction. The inner diameter of the tubes is expanded to 14.95 mm, 15.03 mm and 15.15 mm for 3%, 5% and 7% expansion percentages respectively. An appropriate expansion percentage is needed for building and sustaining the contact pressure between the tube and tubesheet [41,42]. The residual contact pressure and residual stresses that vary with the expansion percentages are key factors affecting joint strength in the roller expansion process [43]. The inner and outer tube surfaces are exposed to forces by the intensity of rolling forces and the development of contact pressure respectively. Fig. 24 demonstrates the microstructures of the inner tube edges at the expanded zone, transition zone and unexpanded zone. The grains at the inner edge of the tube exhibited smaller size spread to a certain depth along a radial direction at the expanded zone. The average grain size of fine grains at the inner tube edge for 3%, 5% and 7% expanded joints at the roller expanded zone are 8.3 μm, 6.25 μm and 5.55 μm respectively. The severity of expansion by 3%, 5%, 7% expansion percentages influenced up to 156 μm, 216.02 μm and 261 μm in depth from the inner tube surface respectively.
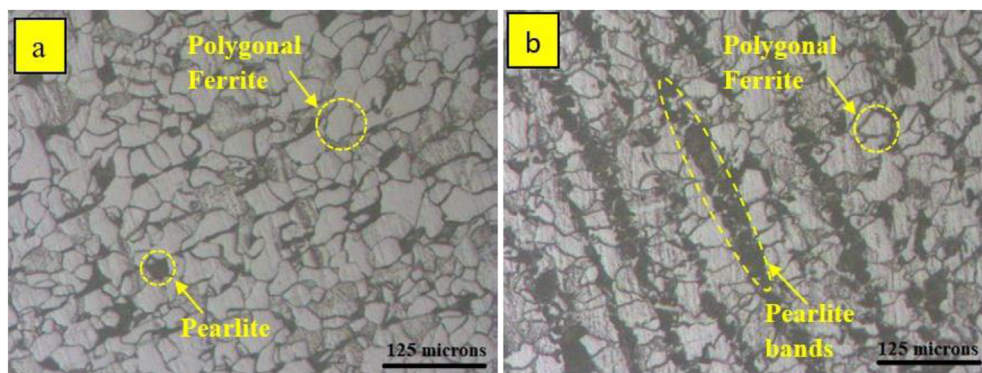
Fig. 16 − Microstructure of (a) ASTM A 179 M tube (b) SA 266 M Gr. 2 tubesheet (200×).
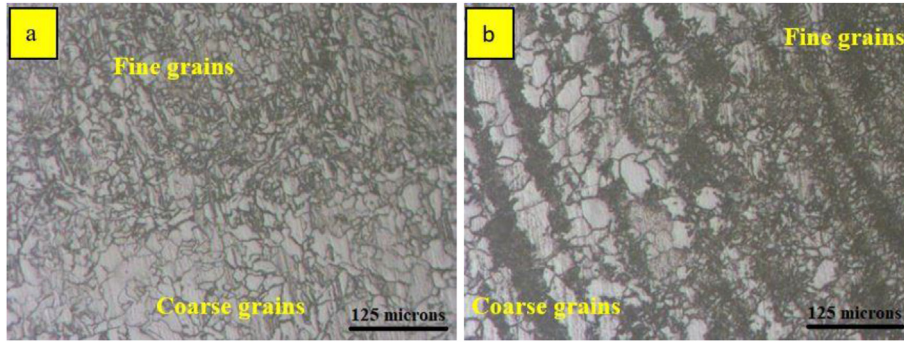
Fig. 17 — Microstructure of (a) tube HAZ (b) tubesheet HAZ (200×).
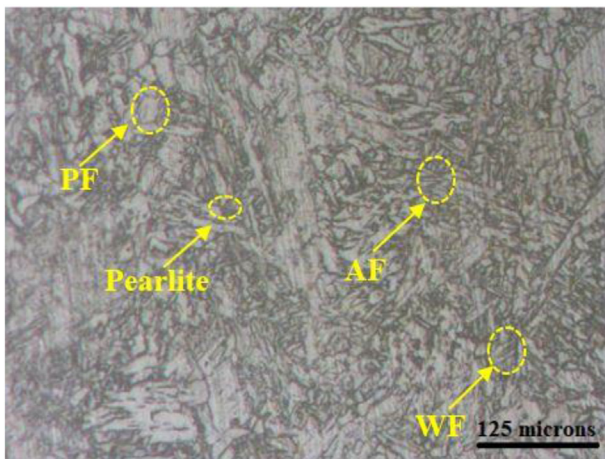
Fig. 18 — Microstructure of weld zone (200×).

The intensity of roller expansion on the inner tube surface was found to have a significant effect on the grain refinement at the expanded zone. Higher the expansion percentage, the finer the grains and the higher the extent of grain refinement from the inner tube surface towards the radially outward direction in the expanded zone. Fig. 25 demonstrates the microstructures of the outer tube edges at the expanded zone, transition zone and unexpanded zone. In the outer tube surfaces, fine grains were observed only on the outer tube surfaces for the 5% and 7% expanded tubes. The grain sizes of 5%

and 7% expanded tubes on the outer tube surface are 10 μm and 8.3 μm whereas the grain size is 12.5 μm for the 3% expanded tubes. In the absence of welding, the minimum expansion percentage required for steel tubes is 5% using roller expansion [44]. The 3% expansion, considered a light expansion, is normally used in combination with the welding operation for ensuring slight contact of the tube with the tubesheet. The lack of distinguishable refinement of grains at the outer tube edge of the 3% expanded tube at the expanded zone indicated that the contact pressure at the tube-to-tubesheet interface is less in the case of light expansion. However, the distinguishable grain refinement was evident for 5% and 7% expansion percentages on the outer tube surface at the expanded zone. The effects of expansion on the grains at the inner and outer tube surfaces of the transition zone and unexpanded zone are negligible. Overall, the grains are found comparatively finer at the roller expanded inner tube surface compared to the outer tube surfaces. Finer grains at the inner tube surfaces indicated that the plastic deformation was dominant by the force exerted by the rollers.

3.6. Hardness

Fig. 26 shows the various regions of interest for hardness measurements. Vickers hardness (HV 10) was evaluated at the tubesheet base material, tubesheet heat affected zone, weld zone, tube base material and tube heat affected zone in accordance with ISO 6507-1 (Fig. 27). The vickers hardness at parent tube and tubesheet materials, heat affected zone and
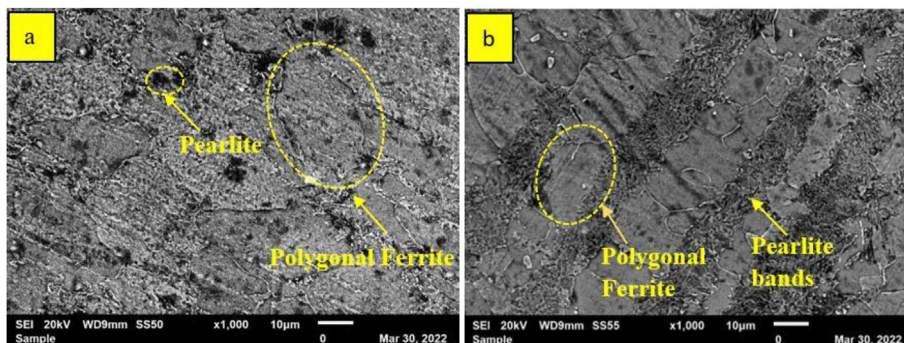
Fig. 19 — SEM microstructure of (a) ASTM A 179 M tube (b) SA 266 M Gr. 2 tubesheet.
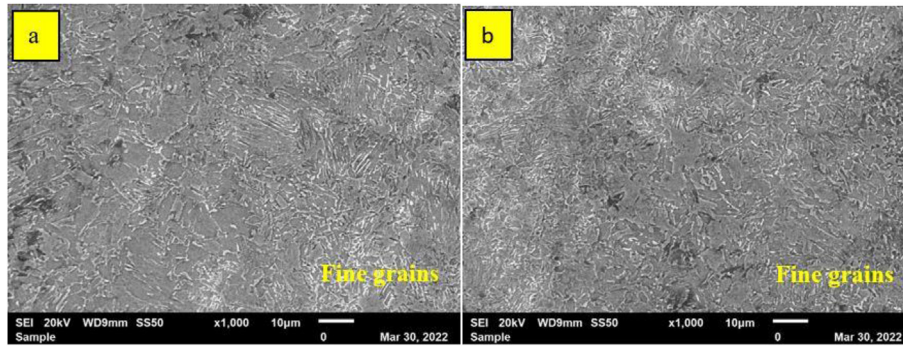
Fig. 20 − SEM Microstructure of (a) tube HAZ (b) tubesheet HAZ.
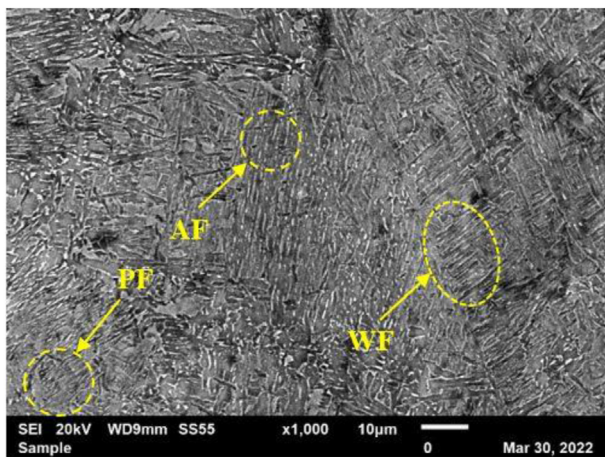
Fig. 21 − SEM microstructure of weld zone.

weld zone were within the acceptable hardness value of 250 HV in accordance with NACE MR0175. According to NACE MR0175, the hardness should be limited to less than 250 HV in welded carbon steels for reducing the susceptibility to the formation of cracks by sulphide stress corrosion (SSC), stress-oriented hydrogen induced cracking and soft zone cracking [45]. Many articles have illustrated the critical role of weld hardness in the failures of heat exchangers. Carlos R Corleto and Argade (2017) discovered that sulfide-assisted stress corrosion cracking, aided by increased weld hardness, was the primary cause of heat exchanger failure. Beer and Johan reported that SA 516 gr. 70 carbon steel with 317 HV was found cracked after being exposed to an H2S environment [46]. With the profound significance of restricting the weld hardness below the critical limit, estimated micro-vickers hardness is provided in Fig. 27. In the current study, the maximum hardness at the weld zone is 221 HV which is below the critical hardness limit of 250 HV for carbon steel welds joints referring to NACE MR0175. The hardness at the weld zone with a mean value of 217.16 HV is comparatively higher than at the heat affected zones and base materials of tube and tubesheet. The alloying elements in the ER 80SNi-1 electrode are intended to enhance the mechanical and metallurgical properties of the welds. In particular, manganese, chromium and vanadium in ER 80SNi-1 electrode increased the hardness at the weld zone [47]. The carbon content has less effect compared to alloying elements in achieving high hardness at the weld zone. In addition, the morphological acicular ferrite and widmanstätten ferrite at the weld zone formed as a result of the cooling process after welding also exhibits higher hardness compared
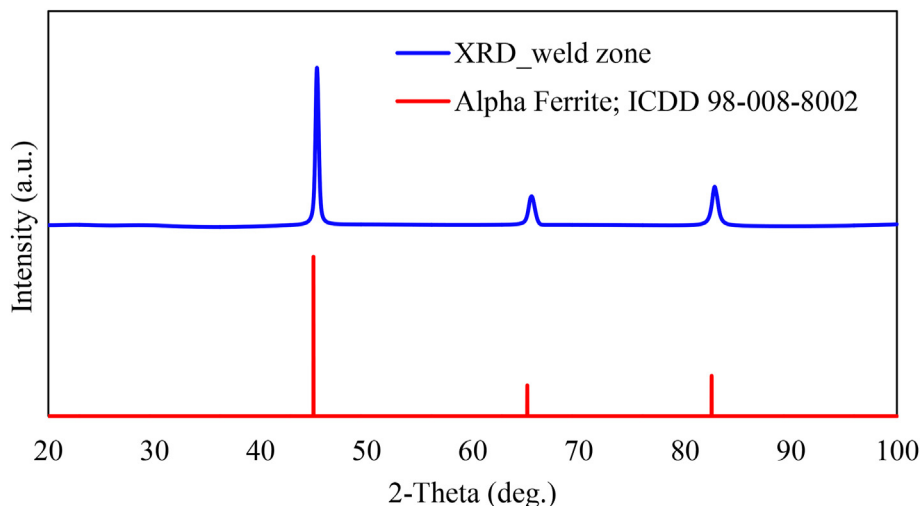
Fig. 22 − XRD analysis of weld zone in TIG welded Tube-to-tubesheet joint.

Table 6 – Elemental composition of the TIG weld zone.

Element	C	Mn	Si	S	P	Cr	Ni	Cu	Ti	Al
%	0.116	1.41	0.573	0.0098	0.0135	0.0567	0.674	0.0755	0.0594	0.0123
Element	N	Mo	V	Nb	W	Pb	Sn	As	Zr	Bi
%	0.0081	0.0299	0.0020	<0.001	<0.005	0.0203	0.0061	0.0125	<0.001	0.0072
Element	Ca	Sb	Se	Te	Ta	B	Zn	Co	Fe	CEV
%	0.00032	0.0509	0.0173	0.0261	<0.007	0.00056	<0.001	<0.001	96.7	0.419

to polygonal ferrite [48]. The average hardness of the tube and tubesheet base materials are 136.3 HV and 167.6 HV. The increased hardness for the SA 266 Gr.2 tubesheet is mainly due to the presence of higher carbon equivalent and pearlite compared to A 179 tube material. The hardness at the heat affected zone was found to be higher than the corresponding tube and tubesheet base materials. The mean hardness at the tube side heat affected zone and tubesheet heat affected zone are 173 HV and 196 HV respectively. The insufficient margin of temperature exceeding the recrystallization temperature and lack of sufficient recrystallization time restrict the coarsening of the grain in the heat affected zone [34]. These fine grains and the thermal stresses substantially increased the hardness in the heat affected zone.

Figs. 28 and 29 show the hardness measured at the expanded zone, transition zone and unexpanded zone of the inner tube surface and outer tube surface. The expansion percentage was found to have a significant effect on the hardness distribution on the inner and outer tube surfaces. On the inner tube surface, the most hardened zone is the expanded zone and the second hardest region is the transition zone applicable for the inspected 3%, 5% and 7% expansion percentages. The hardness at the inner tube surface increased from 164.4 HV to 170.7 HV while increasing the expansion percentage from 3% to 7%. This increase in the hardness was due to the presence of fine grains at the inner tube surface. The finer the grains, the higher the hardness. However, an appreciable change in the hardness was not observed at the transition zone of the inner tube surface. The average hardness at the transition zone decreased from 155.4 HV to 154.6 HV with an increase in the expansion percentage from 3% to 7%.

On the outer tube surface, the hardness at 7% expansion percentage exhibited considerable difference with a peak value of 147.7 HV compared to the 3% and 5% expansion percentages having the hardness of 139 HV and 138.8 HV respectively. The average hardness at the transition zone of 3% and 5% with a value of 144.8 HV and 139.8 HV were greater than the corresponding hardness at the expanded zone. However, the peak hardness at the transition zone was 146.9 HV for the 7% expansion percentage. The 7% expansion percentage was found to influence the hardness in the unexpanded zone close to the transition zone to exhibit 145.6 HV whereas the hardness at the same location for 3% and 5% expanded zones were 138.2 HV and 133.4 HV respectively. The variation in the peak hardness at the expanded zone, transition zone and unexpanded zone at the outer tube surface indicated that the microstructural changes to the outer tube were dependent on the contact pressure building up at the tube-to-tubesheet joint interface.

4. Conclusion

Defect-free high-quality tube-to-tubesheet joints made of ASTM A 179 tubes and SA 266 Gr. 2 tubesheet using hybrid
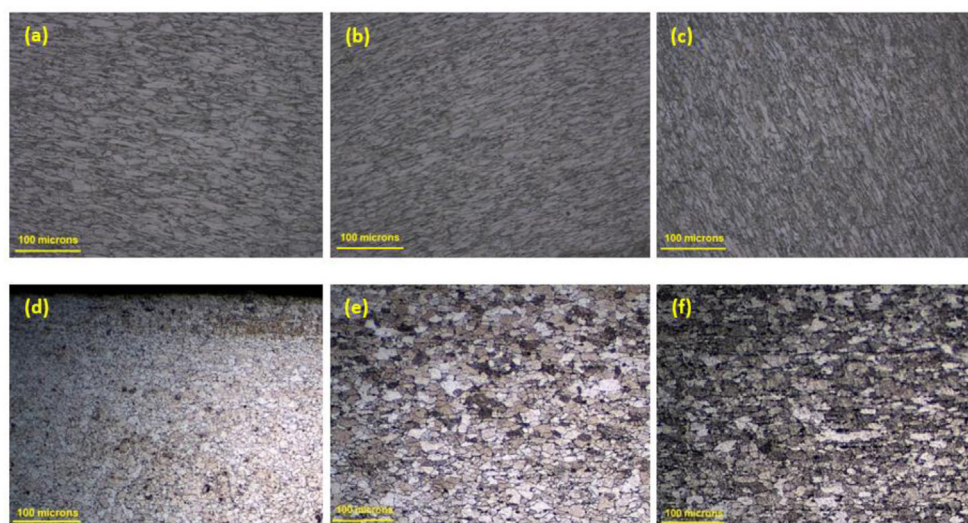
Fig. 23 – Necked region (a) 3% expansion (b) 5% expansion (c) 7% expansion; Expanded zone (d) 3% expansion (e) 5% expansion (f) 7% expansion.
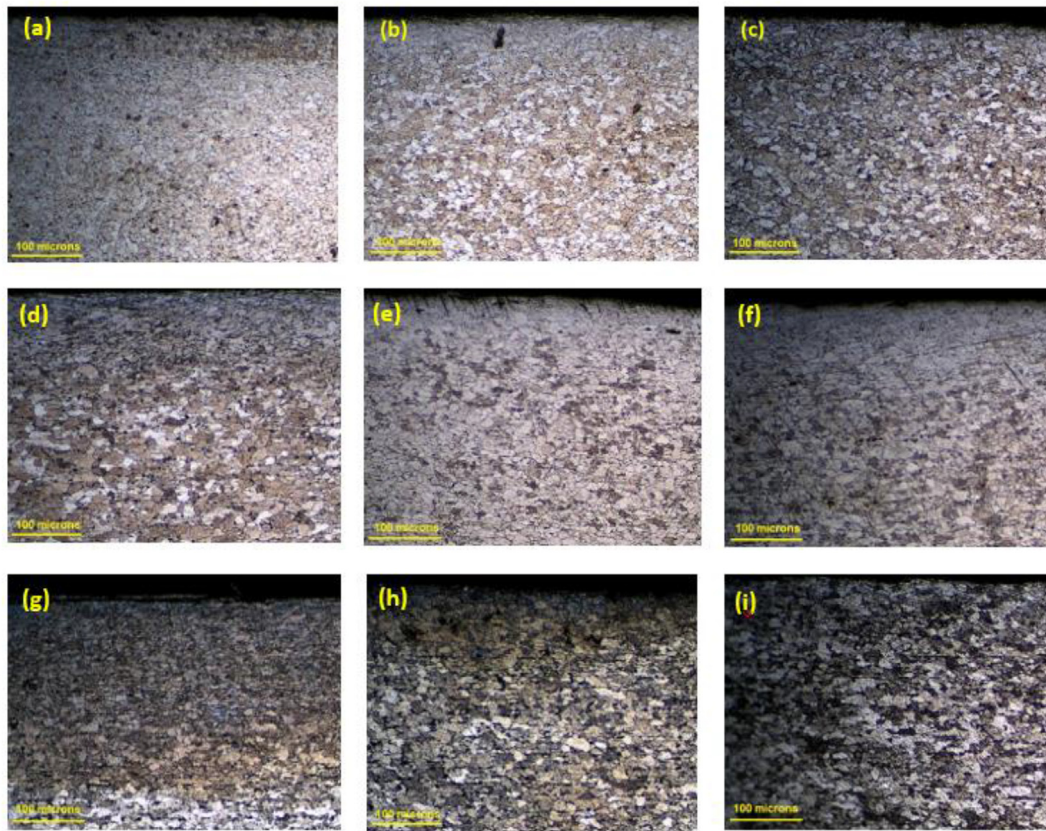
Fig. 24 — Microstructures of inner tube surface at expanded zone, transition zone and unexpanded zone. 3% expansion percentage (a) Expanded zone (b) Transition zone (c) Unexpanded zone; 5% expansion percentage (d) Expanded zone (e) Transition zone (f) Unexpanded zone; 7% expansion percentage (g) Expanded zone (h) Transition zone (i) Unexpanded zone.

tungsten inert gas welding and rolling expansion are produced for investigating the effects of welding and, plastic deformation at 3%, 5% and 7% rolling expansion percentages. The TIG welds of hybrid welded-expanded tube-to-tubesheet joints were qualified with excellent weld fusion and free of surface defects and voids between the root weld and cap weld. The rolling expansion percentages were chosen to investigate the light, moderate and heavy expansion of tubes. The major findings of the study are as follows.

- The minimum leak paths of the welds were greater than two-thirds of the tube wall thickness equals 1.4 mm satisfying the weld throat criteria according to ASME section IX, clause QW-193.1.3. The minimum leak paths were also found greater than the tube wall thickness.
- The tube pull-out loads of hybrid welded-expanded samples with expansion percentages of 3%, 5% and 7% were 41.35 kN, 42.29 kN and 42.19 kN respectively. This closeness of the pull-out loads and tube fracture in the tube pull-out test indicated that the strength of tube-to-tubesheet joints exceeded the axial tube strength.
- Welding followed by 3% expansion was sufficient for producing tube-to-tubesheet joints with joint strength superior to the tube strength.
- The weld zone exhibited high hardness (217.16 HV) due to the presence of alloying elements in the ER 80SNi-1

electrode and by the formation of widmanstätten ferrite at the fusion zone.
- The hardness across the weld was in the order of Weld zone > Tubesheet HAZ > Tube HAZ > Tubesheet > Tube
- The formation of fine grains due to lack of sufficient recrystallization temperature and recrystallization time is the cause for exhibiting comparatively higher hardness at the respective heat affected zones of tube and tubesheet than the corresponding base materials.
- The microstructure of ASTM A179 is equiaxed polygonal ferrite and pearlite colonies whereas the microstructure of SA 266 comprises equiaxed ferrite and banded pearlite. The base materials of the tube and tubesheet have ASTM grain size numbers of ASTM 7 (31.8 μm) and ASTM 8 (22.5 μm). Towards the tube and tubesheet heat affected zones from the base materials, the grain sizes reduced considerably to 9.4 μm (ASTM 10.5) and 7.9 μm (ASTM 11) respectively. The weld zone revealed polygonal ferrite, widmanstätten ferrite (WF) and acicular ferrite (AF).
- The presence of α ferrite (ICDD 98-008-8002) was identified in the weld zone using XRD analysis. The δ ferrite and γ ferrite phases were absent in the weld zone due to the slow cooling rate and low carbon content.
- Plastic deformation at the expanded zone has caused the formation of fine grains and high hardness at both inner and outer tube surfaces. However, the effect of plastic
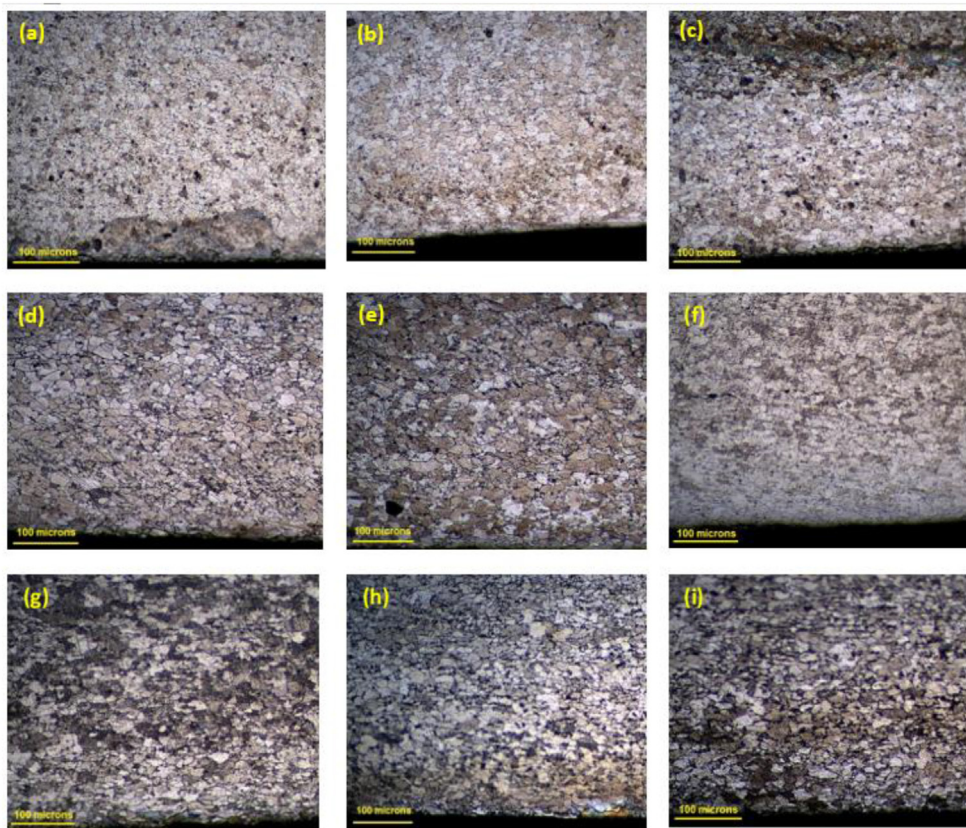
Fig. 25 − Microstructures of outer tube surface at expanded zone, transition zone and unexpanded zone. 3% expansion percentage (a) Expanded zone (b) Transition zone (c) Unexpanded zone; 5% expansion percentage (d) Expanded zone (e) Transition zone (f) Unexpanded zone; 7% expansion percentage (g) Expanded zone (h) Transition zone (i) Unexpanded zone.

deformation and grain refinement was significant at the inner tube surface due to rolling expansion pressures rather than on the outer tube surfaces exposed to contact pressure at the tube-to-tubesheet interface.

- The higher the expansion percentage, the smaller the grains at the inner tube surface and the higher the extent the fine grains are formed from the inner tube surface. The

effect of expansion on the grains at the inner and outer tube surfaces of the transition zone and the unexpanded zone was negligible.

- The absence of grain refinement on the outer tube surface using light expansion at a 3% expansion percentage indicated that the contact pressure was inadequate at the tube-to-tubesheet interface.
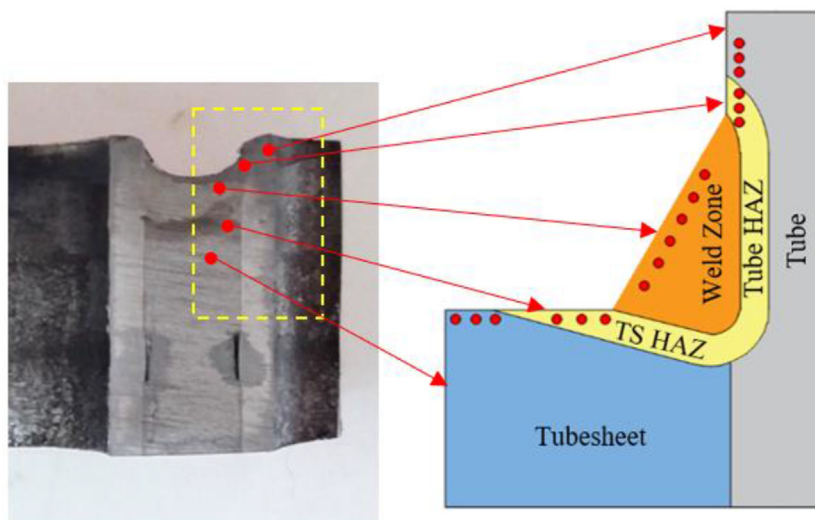
Fig. 26 − Region of interest for hardness measurements.
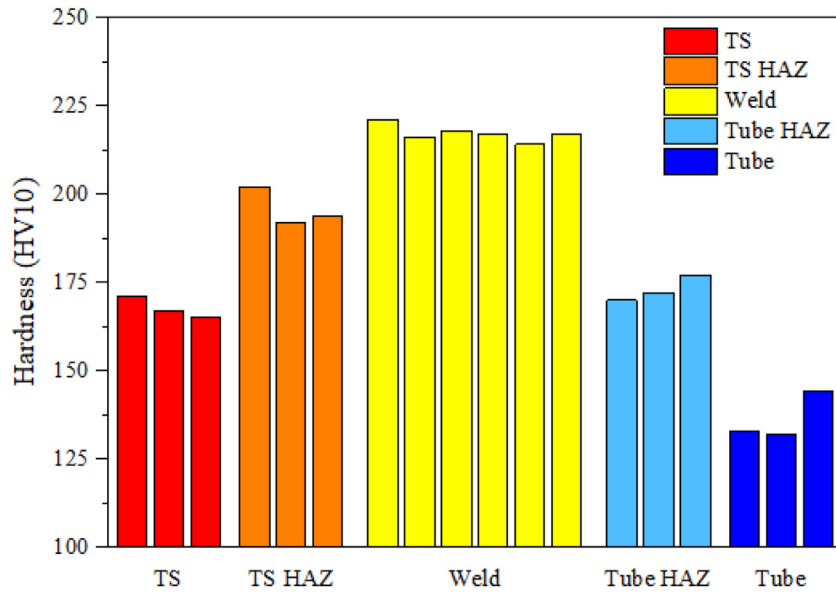
Fig. 27 – Vickers hardness at weld.
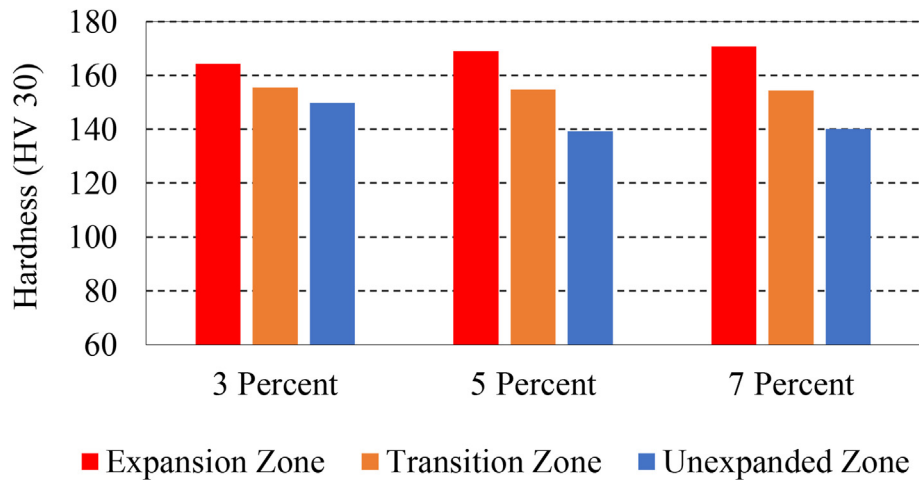
Fig. 28 – Vickers hardness at the inner tube surface.
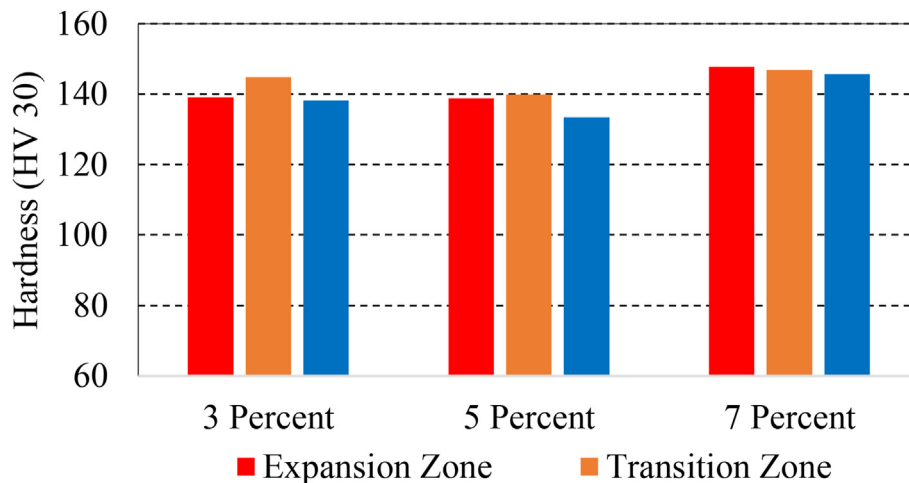
Fig. 29 – Vickers hardness at the outer tube surface.

- The hardness at the expanded zone and transition zone of the inner tube surface was higher than at the outer tube surface as a result of extensive tube wall thinning and plastic deformation.

Funding

Availability of data and material

Data are presented inside the paper. Any data could also be provided based on the request to corresponding author.

Code availability

No codes are used.

Ethics approval

N/A.

Consent to participate

N/A.

Consent for publication

N/A.

Authors' contributions

Dinu Thomas Thekkuden: Investigation, Methodology, Resources, Writing − original draft, Data curation, Visualization, Validation. Abdel- Hamid I. Mourad: Conceptualization, Writing − original draft, Writing − review & editing, Visualization, Validation, Supervision, Project administration, Methodology, Investigation, Funding acquisition, Formal analysis. Tholkappiyan Ramachandran: Resources. Abdel-Hakim Bouzid: Investigation, Writing - Review & Editing, Supervision, Visualization, Validation. Ravi Kumar: Investigation, Validation, Supervision, Writing - Review & Editing. Ahmed Alzamly: Resources.

Declaration of Competing Interest

The authors declare that they have no known competing financial interests or personal relationships that could have appeared to influence the work reported in this paper.

REFERENCES

[1] Ali M, Ul-Hamid A, Alhems LM, Saeed A. Review of common failures in heat exchangers—Part I: mechanical and elevated temperature failures. Eng Fail Anal 2020;109:104396.

[2] Xu S, Wang C, Wang W. Failure analysis of stress corrosion cracking in heat exchanger tubes during start-up operation. Eng Fail Anal 2015;51:1—8.

[3] Alzafin YA, Mourad A-H, Abou Zour M, Abuzeid OA. Stress corrosion cracking of Ni-resist ductile iron used in manufacturing brine circulating pumps of desalination plants. Eng Fail Anal 2009;16:733—9.

[4] Saffiudeen MF, Syed A, Mohammed FT. Failure analysis of heat exchanger using internal rotary inspection system (IRIS). J Fail Anal Prev 2021;21:494—8.

[5] Yang X-L, Gong Y, Yang Z-G. Failure analysis on abnormal leakage between tubes and tubesheet of spiral-wound heat exchanger for nuclear power plant. Eng Fail Anal 2020;118:104900. https://doi.org/10.1016/j.engfailanal.2020.104900.

[6] Adullah S, Ezuber HM. Repair of tube—tubesheet weld cracks in a cracked gas/steam heat exchanger. J Fail Anal Prev 2011;11:611—7.

[7] Gong Y, Ma F-Q, Xue Y, Jiao C-S, Yang Z-G. Failure analysis on leaked titanium tubes of seawater heat exchangers in recirculating cooling water system of coastal nuclear power plant. Eng Fail Anal 2019;101:172—9.

[8] Liu L, Ding N, Shi J, Xu N, Guo W, Wu CML. Failure analysis of tube-to-tubesheet welded joints in a shell-tube heat exchanger. Case Stud Eng Fail Anal 2016;7:32—40. https://doi.org/10.1016/j.csefa.2016.06.002.

[9] Huang T, Zhang G, Liu F. Design, manufacturing and repair of tube-to-tubesheet welds of steam generators of CPR1000 units. Nucl Eng Des 2018;333:55—62.

[10] Shankar AR, Sole R, Thyagarajan K, George RP, Mudali UK. Failure analysis of titanium heater tubes and stainless steel heat exchanger weld joints in nitric acid loop. Eng Fail Anal 2019;99:248—62.

[11] Corleto CR, Argade GR. Failure analysis of dissimilar weld in heat exchanger. Case Stud Eng Fail Anal 2017;9:27—34.

[12] Sui R, Zhao Y, Ge B, Wang W. Failure analysis of leakage at tube-to-tubesheet joints of a waste heat boiler. Eng Fail Anal 2021;129:105639.

[13] Thekkuden DT, Mourad A-HI, Bouzid A-H. Failures and leak inspection techniques of tube-to-tubesheet joints: a review. Eng Fail Anal 2021;130:105798.

[14] Shuaib AN, Duffuaa OM, Merah N, Al-Nassar Y. Residual stresses in roller expanded tube-tubesheet joints with large initial clearance and grooves. J Press Vessel Technol 2011;133:51211—7. https://doi.org/10.1115/1.4003465.

[15] Bouzid A-H, Pourreza M. Analysis of residual stresses in the transition zone of tube-to-tubesheet joints. J Press Vessel Technol 2019:141.

[16] Saffiudeen MF, Mohammed FT, Syed A. A case study on procedure standardization of heat exchanger retubing in KSA oil and gas industries. J Fail Anal Prev 2020;20:1451—5.

[17] Massey KM, Jones MW. Tube pullout testing experience. California, USA: Proc. ASME 2012 Power Conf.; 2012. p. 1—9. https://doi.org/10.1115/ICONE20-POWER2012-55186.

[18] Thekkuden DT, Mourad A-HI, Bouzid A-H. Impact of grooves in hydraulically expanded tube-to-tubesheet joints. In: ASME 2020 Press. Vessel. Pip. Conf., American Society of Mechanical Engineers Digital Collection; 2020.

[19] Allam M, Bazergui A. Axial strength of tube-to-tubesheet joints: finite element and experimental evaluations. J Press Vessel Technol 2002;124:22. https://doi.org/10.1115/1.1398555.

[20] Haneklaus N, Reuven R, Cionea C, Hosemann P, Peterson PF. Tube expansion and diffusion bonding of 316L stainless steel tube-to-tube sheet joints using a commercial roller tube expander. J Mater Process Technol 2016;234:27—32. https://doi.org/10.1016/j.jmatprotec.2016.03.008.

[21] Ma H, Yu HJ, Qian CF, Liu ZS, Zhou JX. Experimental study of hydraulically expanded tube-to-tubesheet joints for shell-and-tube heat exchangers. Proc Eng 2015;130:263—74. https://doi.org/10.1016/j.proeng.2015.12.220.

[22] Thekkuden DT, Mourad A-HI, Bouzid A-H, Darabseh T. Impact of expansion pressure on wall thinning and contact pressure for hydraulically expanded tube-to-tubesheet joints: numerical analysis.. In: 2020 Advances in Science and Engineering Technology International Conferences; 2020. p. 1—6.

[23] Wei XL, Ling X. Investigation of welded structures on mechanical properties of 304L welded tube-to-tubesheet joints. Eng Fail Anal 2015;52:90—6.

[24] Zeng Q, Li Y, Zhang G, Shi J, Li C, Zhang Z, et al. Influence of neighbouring tube expansion on the residual stress of tubesheet with single-row holes. Int J Press Vessel Pip 2022;197:104651.

[25] Bouzid A-H, Zhu L. A study of neighbouring tube expansion effect on the residual contact pressure of tube-to-tubesheet joints. Int J Press Vessel Pip 2018;165:185—92.

[26] Saffiudeen MF, Mohammed FT, Syed A. Comparative study of tube to tubesheet welding qualification on heat exchanger. J Eng Appl Sci 2022;69:1—14.

[27] Boiler A, Code PV. Section IX: welding and brazing qualifications. Paragraph QW-290, temper bead welding. ASME; 2004. p. 48—50.

[28] Boiler A, Code PV. Section VIII: rules for construction of pressure vessels, Division 1. New York: Am Soc Mech Eng (ASME); 2019. p. 585—91.

[29] Yokell S. Assuring tube-to-tubesheet joint tightness and strength. J Press Vessel Technol 2012:134.

[30] Sang ZF, Zhu YZ, Method E. Reliability factors and tightness of tube-to-tubesheet joints. J Press Vessel Technol 1996;118:137—41.

[31] Kumar P, Pai A. An overview of welding aspects and challenges during manufacture of intermediate heat exchangers for 500MWe prototype fast breeder reactor. Proc Eng 2014;86:173—83. https://doi.org/10.1016/j.proeng.2014.11.026.

[32] Muhayat N, Matien YA, Sukanto H, Saputro YCN. Fatigue life of underwater wet welded low carbon steel SS400. Heliyon 2020;6:e03366.

[33] Mohsenzadeh MS, Mazinani M. On the yield point phenomenon in low-carbon steels with ferrite-cementite microstructure. Mater Sci Eng A 2016;673:193—203.

[34] Zhao Y, Wang Q, Chen H, Yan K. Microstructure and mechanical properties of spray formed 7055 aluminum alloy by underwater friction stir welding. Mater Des 2014;56:725—30.

[35] Madariaga I, Gutierrez I, García de Andrés C, Capdevila C. Acicular ferrite formation in a medium carbon steel with a two stage continuous cooling. Scripta Materialia 1999;41(3):229—35.

[36] Mourad AHI, Khourshid A, Sharef T. Gas tungsten arc and laser beam welding processes effects on duplex stainless steel 2205 properties. Mater Sci Eng A 2012;549:105—13. https://doi.org/10.1016/j.msea.2012.04.012.

[37] Glišić D, Radović N, Drobnjak D, Fadel A. Critical stress for cleavage fracture in continuously cooled medium carbon V-microalloyed steel. Proc Mater Sci 2014;3:1226—31.

[38] İrsel G. Study of the microstructure and mechanical property relationships of shielded metal arc and TIG welded S235JR steel joints. Mater Sci Eng A 2022;830:142320.

[39] Bhadeshia H, Svensson LE. Modelling the evolution of microstructure in steel weld metal. Math Model Weld Phenom 1993;1:109—82.

[40] Ashrafi H, Shamanian M, Emadi R, Ghassemali E. Void formation and plastic deformation mechanism of a cold-rolled dual-phase steel during tension. Acta Metall Sin (English Lett 2020;33:299—306.

[41] Bouzid AH, Mourad AHI, El Domiaty A. Influence of Bauschinger effect on the residual contact pressure of hydraulically expanded tube-to-tubesheet joints. Int J Press Vessel Pip 2016;146:1—10. https://doi.org/10.1016/j.ijpvp.2016.07.002.

[42] Kalnins A, Updike DP, Caldwell SM. Contact pressure in rolled tube-tubesheet joints. Nucl Eng Des 1991;130:229—34. https://doi.org/10.1016/0029-5493(91)90131-Z.

[43] Al-Aboodi A, Merah N, Shuaib AR, Al-Nassar Y, Al-Anizi SS. Modeling the effects of initial tube-tubesheet clearance, wall reduction and material strain hardening on rolled joint strength. J Press Vessel Technol 2008:130.

[44] Basic guidelines of tube expanding n.d. https://www.tcwilson.com/t/tube-rolling-basic-guidelines.

[45] Milliams DE, Cottage D, Tuttle RN. ISO 15156/NACE MR0175-A new international Standard for metallic materials for use in oil and gas production in sour environments. Corros; 2003. OnePetro; 2003.

[46] Beer D, Johan D. The relationship of weld metal hardness residual stress and susceptible to stress corrosion cracking in hydrogen sulphide environment in A516 Grade 70 carbon steel shielded metal arc welded joint. 2019.

[47] Bose-Filho WW, Carvalho ALM, Strangwood M. Effects of alloying elements on the microstructure and inclusion formation in HSLA multipass welds. Mater Char 2007;58:29—39.

[48] Cho Y, Lee J, Kim D, Kang J, Choo WY, Han HN. Ferrite phase analysis based on low-angle grain boundary density in low carbon linepipe steel. Proc 5th Int Symp Steel Sci (ISSS 2017) 2017:203. 6.